



Highly sensitive and stable yolk-shell Bi₂MoO₆ gas sensor for ppb-level isopropanol detection

Chao Zhang^{a,*}, Xiaoxi He^a, Yiwen Zhou^a, Jinyong Xu^a, Zichen Zheng^a, Yixiang Bian^a, Marc Debligny^b

^a College of Mechanical Engineering, Yangzhou University, Yangzhou 225127, China

^b Service de Science des Matériaux, Faculté Polytechnique, Université de Mons, Mons 7000, Belgium

ARTICLE INFO

Keywords:

Bi₂MoO₆
Yolk-shell
Gas sensor
Isopropanol

ABSTRACT

Metal oxide semiconductor used for the fabrication of volatile organic gas sensors has gained significant popularity in recent years. This paper discusses the synthesis of yolk-shell-structure Bi₂MoO₆ (YS-BMO) for isopropanol detection through quasi-molecular imprinting-based solvent-thermal methods. Various qualitative characterization techniques, gas sensing performance tests, and theoretical calculations collectively indicate that YS-BMO with molecular imprinting is a potential material for isopropanol sensing. YS-BMO with an average diameter of approximately 1.5 μm (15 h of solvothermal), demonstrates impressive isopropanol detection capabilities, a practical detection limit of 100 ppb, along with suitable response and recovery times. Density functional theory (DFT) calculations provide a deeper understanding and analysis of the response mechanism of Bi₂MoO₆ to isopropanol, considering aspects such as band structure, electron transfer, and adsorption energy.

1. Introduction

Breath gas diagnosis utilizing gas sensors made of metal oxide semiconductor has recently emerged as a research hotspot for cost-effectiveness, user-friendliness, and real-time detection capabilities [1, 2]. The volatile organic compounds (VOCs) in exhaled breath are detected to indicate potential diseases via gas sensors [3]. Variety VOCs such as isopropanol, toluene, 2-butanone, and formaldehyde, are considered as biomarkers for the diagnosis of lung cancer. We selected isopropanol (C₃H₈O) for its average concentration of about 398 ppb in the bodies of lung cancer patients, which is twice as much as in healthy individuals (169 ppb) [4,5]. Generally, human exhaled breath has an elevated relative humidity (RH), which can be a huge challenging for MOS gas sensors [6]. Exploring high-performance gas-sensitive materials for detecting isopropanol at ppb levels in high humidity conditions is of utmost importance.

γ-Bi₂MoO₆ is a typical metallurgical perovskite-type composite oxide, exhibiting excellent electrochemical properties. It has received extensive attention in various fields including photocatalysts, high-performance capacitors, and others [7–10]. It is worth noting that Bi₂MoO₆ is composed of [Bi₂O₂]²⁺ layers and [MoO₄]²⁻ octahedra. The open and stable interlayer channels are particularly suitable for charge

separation and transfer [11]. Bi₂MoO₆ has a bandgap of approximately 2.6–2.8 eV making it a promising candidate for applications in various fields [12]. Perovskite-type [MoO₄]²⁻ layers in Bi₂MoO₆ have an octahedral shared structure that allows for efficient electron ionization and excellent gas sensitivity [13]. Liu et al. successfully fabricated 5% Ag-doped Bi₂MoO₆ through a solvothermal and glucose reduction technique with excellent NH₃ gas-sensing performance, including limit of detection (50 ppb), long-term stability, and a response of 37.6–200 ppb NH₃ [14]. Zhang et al. successfully synthesized Bi₂MoO₆/ZnO with unique structure for butanol detecting through a hydrothermal method [12]. Cui and Zhang et al. synthesized flower-like and walnut-like Bi₂MoO₆, which can both detect 0.1 ppb H₂S at a relatively low working temperature (around 150 °C), and almost unaffected by air humidity [15,16]. These studies demonstrated the significant stability, response, and humidity insensitivity of the Bi₂MoO₆ material due to the unique structure.

Various synthetic strategies have been employed to produce Bi₂MoO₆ with distinct morphologies [17,18], such as nanosheets [19–21], nanoneedle [22], flower-like [23,24], hollow sphere [25–27], walnut-like [16] and yolk-shell structure [28]. Yolk-shell structure allows for the penetration and diffusion of VOCs due to its porous thin shell. And its larger specific surface area (SSA) means more contact

* Correspondence to: College of Mechanical Engineering, Yangzhou University, Huayang West Road 196, Yangzhou 225127, Jiangsu, China.

E-mail address: zhangc@yzu.edu.cn (C. Zhang).

points that can improve gas sensing efficiency, enhance sensitivity, and potential selectivity and stability. The unique combination of these structures makes Bi_2MoO_6 particularly effective in gas sensors [29]. Currently, there are many sensors based on yolk-shell structures, such as LaFeO_3 [29], CeO_2 [30], ZnCo_2O_4 [31], $\alpha\text{-Fe}_2\text{O}_3$ [32] and $\text{SnO}_2\text{-TiO}_2$ [33].

The current study proposes a solvothermal process combined with quasi-molecular imprinting method (QMIM) to synthesize Bi_2MoO_6 with controllable yolk-shell. Using 1,2-propanediol as a solvent act as killing two birds with one stone: it exhibits a molecular structure akin to isopropanol, which enhances the selectivity towards isopropanol, and it also allows for the synthesis of YS-BMO. Gas sensors based on YS-BMO are expected to demonstrate significantly superior gas-sensing performance towards low-concentration isopropanol under high RH compared to plate-like or hollow sphere Bi_2MoO_6 . This article focuses on exploring the gas-sensing performance and gas-sensing mechanism of isopropanol under different operating conditions.

2. Experimental section

2.1. Sample preparation

Solvothermal method combined with QMIM was used to prepare YS-BMO. Initially, 4 mM $\text{Bi}(\text{NO}_3)_3 \cdot 5 \text{H}_2\text{O}$ and 2 mM $\text{C}_{10}\text{H}_{14}\text{MoO}_6$ were dissolved into 10 mL of 1,2-propanediol under magnetic stirring separately. Then, the two solvents and 60 mL of ethanol were blended slowly and uniformly while stirring. Transfer the homogeneous liquid into a 100 mL high-pressure reactor and heated to 160 °C for 15 h. Centrifuged the products three times with deionized water and ethanol after natural cooling, respectively, and dried at 80 °C for 12 h. Then annealed the dried powder at 400 °C for 2 h, forming a bright yellow monodisperse microspheres as finished products. Bi_2MoO_6 prepared with different solvothermal durations (x hours, x = 1, 3, 6, 9, 12, 15, 18, 21) is named as S-x. All chemicals information is provided in the ‘‘Supplementary Materials’’.

2.2. Characterization

Characterizations of Bi_2MoO_6 powders were performed using field-emission scanning electron microscopy, energy-dispersive X-ray spectroscopy (FESEM, EDS, GeminiSEM 300), and high-resolution transmission electron microscopy (HRTEM, Hitachi HT7800). The phase composition was determined by X-ray diffraction (XRD) with $\text{Cu-K}\alpha$ (1.54184 Å) radiation at 30 kV and 25 mA using Bruker-AXS D8 Advance. X-ray photoelectron spectroscopy (XPS, ThermoFisher Scientific Escalab250Xi) was employed to investigate the presence and chemical state of lattice oxygens. SSA was measured under the Barret-Emmett-Teller (BET) method based on nitrogen adsorption isotherms using a Quadrasorb EVO instrument at 300 °C.

2.3. Fabrication and measurement of gas sensor

The sensors were formed by firmly depositing a uniform suspension of Bi_2MoO_6 powder and deionized water on the electrode (Pt integrated Al_2O_3 substrate electrodes, purchased from Wuhan Huachuang Ruike Co., Ltd.). The substrates were settled at room temperature for several days before measurement to improve measurement stability. As shown in Fig. S1, three mass flow controllers (MFC) were used during the testing process to inject standard air with a certain humidity and target VOCs into testing chamber. VOC is brought out of solution through a wash bottle and further diluted to the target concentration using MFCs before reaching the testing chamber. The total mass flow through MFCs is 800 mL/min. And the saturation concentration of VOCs is calculated by formula (1) at 25 °C [34]. The control method and measurement results (Fig.S4) of relative humidity are presented in ‘‘Supplementary Materials’’.

$$\text{Concentration (ppm)} = 10^{-3} \times (D \times \rho / m / K_H) \quad (1)$$

Where D ($\mu\text{L/L}$) represents the amount of solvent added to the solution, ρ represents solvent density, m represents the molecular weight of the solvent, K_H represents Henry’s law. More details can be found in ‘‘Supplementary Materials’’.

The stable resistance (R) obtained in humid standard air is marked as R_a , while the stable resistance obtained in the target gas is marked as R_g . The sensor response (S) is defined by $S = (R_a/R_g) - 1$. The response time (t_{res}) and recovery time (t_{rec}) corresponded to the time taken for the resistance to reach 90% of the maximum resistance change.

3. Results and discussion

3.1. Characterization result

The XRD pattern of S-15 in Fig. 1a illustrates the properties of YS-BMO as a highly crystalline powder, showing narrow and sharp peaks. It displays various distinct diffraction peaks at 2θ of 28.25°, 32.61°, 47.15°, 55.56° and 58.43°, which match well with the (131), (002), (151), (062), (331), (133) crystal planes of the JCPDS No.72–1524. Furthermore, Fig. 1b provides the XRD spectra of S-1, S-3, S-6, S-9, S-12, S-18, and S-21, which are compared to distinguish the differences between these materials. It reveals that when subjected to a solvothermal treatment for less than 3 h, the material produced is Bi_2O_3 , and its diffraction peak reveals correspondences with JCPDS No.78–1793. When solvothermal treatment exceeds 6 h, the obtained materials are Bi_2MoO_6 . The XRD spectra of Bi_2MoO_6 showed no corresponding peaks to impurities, indicating that the powder is highly crystalline Bi_2MoO_6 . Remarkably, the XRD spectra demonstrates that the crystallinity of Bi_2MoO_6 intensifies as the solvothermal treatment time increased. Nevertheless, when the solvothermal treatment surpasses 21 h, the key peak found at 28.25° begins to bifurcate. This phenomenon is due to excessive grain growth induced by the extended solvothermal treatment leading to a significant internal stress within the crystal grains. The average grain size of S-x (x = 1, 3, 6, 9, 12, 15, 18, 21) was calculated by Debye-Scherrer formula, which were 4.652 nm, 8.960 nm, 8.819 nm, 9.915 nm, 13.938 nm, 10.622 nm, 12.271 nm, and 14.103 nm, respectively. It was found that the grain size showed an increasing trend with solvothermal time, and the grain size of S-15 was in the best state. And during the calculation process, we observed that S-21 not only possesses the largest average grain size but also exhibits more significant variations in grain sizes across different crystal facets. This observation aligns with the excessive growth theory we discussed. We aim to demonstrate this in our forthcoming research works.

To obtain more precise details about the inherent properties of YS-BMO, Raman spectra were measured by employing a UV-Vis spectrometer, as depicted in Fig. 1c. Bi_2MoO_6 is observed to have absorption spectra in a wide region due to its narrow band gap width. Moreover, according to the inset of Fig. 1c, S-15 and S-12 are found to have stronger light absorption than samples S-3, 6, 9, and 18, because their unique yolk-shell structures [28]. By plotting the Tauc curve using the formula (2) [35,36], we calculated the experimental bandgap of S-15 to be about 2.73 eV.

$$(ahv)^2 = K(hv - E_g) \quad (2)$$

Fig. 1d-e display the distinctive yolk-shell structure of S-15. According to the measurements, Bi_2MoO_6 microspheres, ranging in diameter from 1 to 2 μm , are evenly distributed. High magnification SEM image of the fractured microsphere particles (Fig. 1e) demonstrates that the resultant YS-BMO has a layered structure. The shell is formed by nanoscale flakes and has a thickness of around 150 nm. The yolk (nucleus) is assembled by the tight packing of smaller nanoparticles, with a relatively dense surface. The core-shell layered structure of yolk-shell is particularly noteworthy, as it remarkably amplifies the SSA of Bi_2MoO_6 .

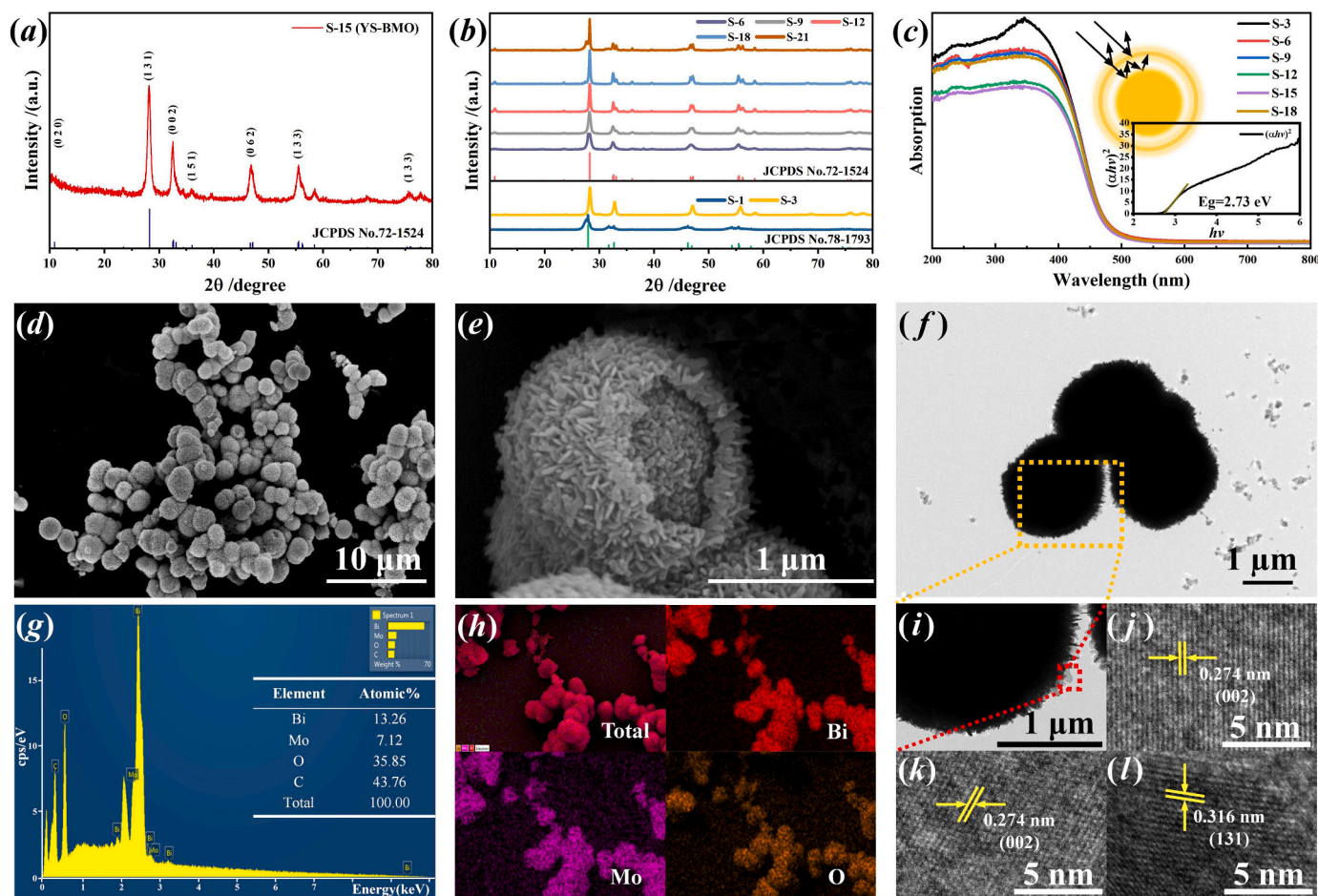


Fig. 1. (a-b) XRD pattern of Bi_2MoO_6 . (c) UV-Vis absorption spectra of Bi_2MoO_6 . (d-e) SEM and (f) TEM images of YS-BMO. (g-h) EDS Mapping of YS-BMO. (i-l) HRTEM images of YS-BMO.

and enhances gas adsorption sites, thereby boosting its gas-sensing property [37]. Yolk-shell structure creates open and stable large inter-layer channels that enhance the penetration, diffusion, and adsorption of the target VOC molecules, thereby enhancing response speed. EDS in Fig. 1 g indicate that the atomic ratio of Bi to Mo in S-15 is nearly 2:1, confirming that the sample is $\gamma\text{-Bi}_2\text{MoO}_6$ corresponding to the XRD results, rather than the α and β phases. Fig. 1 h exhibits the uniform distribution of Bi, Mo, O element. The high magnification HRTEM image of YS-BMO, depicted in Fig. 1 f, i-l, illustrates the particles' regular spherical structure. Furthermore, the lattice stripes with an interplanar distance of 0.274, and 0.316 nm can be assigned to the (002) and (131), respectively, of JCPDS No.72-1524 [38].

To comprehend the formation mechanism of YS-BMO, the formation process at various solvothermal synthesis duration were explored. Fig. 2a-h show high magnification SEM images of Bi_2MoO_6 prepared at 160 °C for different solvothermal duration. Fig. S2 outlines the structure formation process of YS-BMO microspheres. With increasing solvothermal duration, a progression is observed in the formation of uniform and smooth porous microspheres, followed by rough, porous microspheres, hollow Bi_2MoO_6 spheres with thicker shells, thin-walled hollow spheres, the initial formation of yolk-shell structures, the development of ideal yolk-shell structures, and ultimately, the excessive growth and fusion of cores and shells. After the solvothermal exceeds 21 h, the Bi_2MoO_6 nanoparticles grow excessively and lose the desired morphology as shown in Fig. 2 h, which is consistent with the conclusion obtained in XRD characterization. Interestingly, during the structural growth process, the diameter of the outer shell hardly changed. The yolk-shell growth mechanism of Bi_2MoO_6 proposed from the high

magnification SEM images was similar to the report by Li [39]. The growth mechanism analysis of YS-BMO is provided in "Supplementary Materials". Fig. 2i shows additional Bi_2MoO_6 nanosheets synthesized by hydrothermal method [40]. Bi_2MoO_6 nanosheets are the basis for composing the YS-BMO, but due to the lack of growth driving force of solvent, spherical shape was not formed. Table 1 lists the SSA and average pore size of S-x (x = 3, 6, 9, 12, 15, 18), and S-15 has the largest SSA. Interestingly, S-6 exhibits the largest average pore size. We speculate that rapid grain growth occurs during this reaction step, leading to the formation closed pores of smaller pores, which results in the measured average pore size being skewed towards larger values. The inference is based on our analysis of corresponding SEM images and pore size distribution curves. Detailed analysis can be found in the "Supplementary Materials".

Furthermore, the chemical states and oxygen species of S-15 (YS-BMO) were characterized by XPS. The spectra obtained are expressed in Fig. 3a. The reported spectra show the presence of Bi, Mo, and O species in YS-BMO. Fig. 3b indicates two peaks at 158.49 eV and 163.79 eV, respectively, corresponding to $\text{Bi}^{3+} 4f_{7/2}$ and $\text{Bi}^{3+} 4f_{5/2}$ orbital of YS-BMO [41]. The spin-orbit splitting of the two peaks is 5.3 eV, suggesting that Bi is present in Bi^{3+} . The Mo 3d spectrum (Fig. 3c) is nearly identical to the Bi 4f spectrum. The $\text{Mo}^{6+} 3d_{3/2}$ and $\text{Mo}^{6+} 3d_{5/2}$ are detected at 234.91 eV and 231.77 eV. The spin-orbit splitting indicates an oxidation state of +6 for Mo atoms. Moreover, Fig. 3d demonstrates the resolution of the O1s spectrum into two Gaussian-Lorentz peaks detected at 529.23 eV and 529.62 eV, corresponding to Bi-O and Mo-O [23].

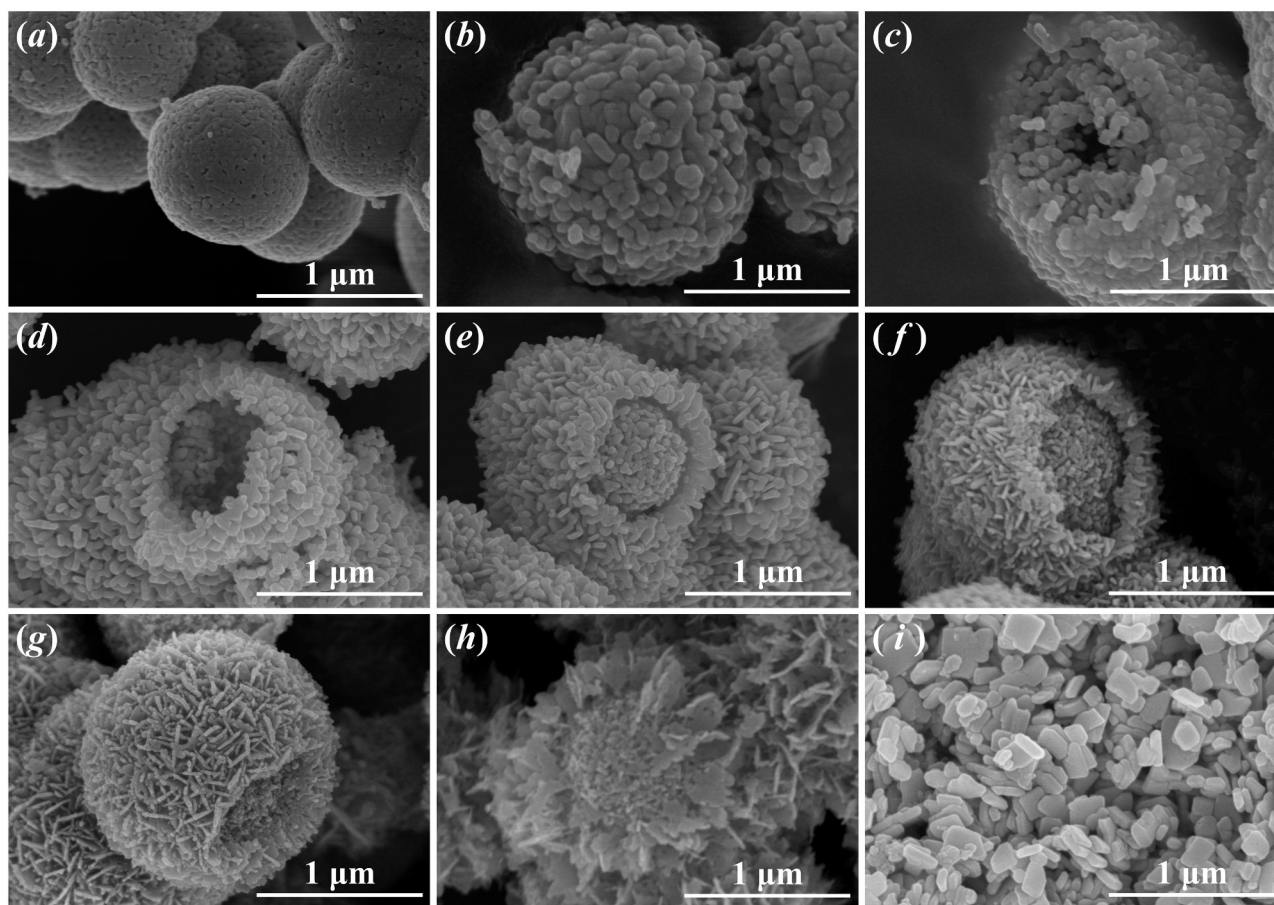


Fig. 2. (a–h) SEM images of Bi_2MoO_6 prepared at solvothermal time of 1 h, 3 h, 6 h, 9 h, 12 h, 15 h, 18 h and 21 h, respectively. (i) SEM of Bi_2MoO_6 nanosheets.

Table 1

The specific surface area and average pore size of Bi_2MoO_6 particles.

Sample	Specific surface areas ($\text{m}^2\cdot\text{g}^{-1}$)	Average pore size (nm)
S-3	13.148	13.140
S-6	15.700	18.232
S-9	19.737	13.130
S-12	25.098	12.273
S-15	35.121	17.164
S-18	32.085	13.932

3.2. Gas sensing performance

The gas sensitivities of 5 ppm isopropanol on Bi_2MoO_6 samples prepared with varied solvothermal durations are tested in this study. As shown in Fig. 4a, S-15 with yolk-shell structures exhibited the highest response. The response demonstrated a nearly identical trend to the specific surface areas presented in Table 1. The yolk-shell structure was advantageous because it efficiently amplified the SSA of nanoparticles and provided an increased number of contact sites for adsorbed oxygen. The special interlayer structure of the yolk-shell also notably facilitated the penetration and diffusion of isopropanol gas molecules [42]. In addition, S-12 with early yolk-shell structure also shows better response to 5 ppm isopropanol than other structures of Bi_2MoO_6 , which proves that the strategy of synthesizing yolk-shell structure to enhance the isopropanol gas sensitivity of Bi_2MoO_6 was successful. Further studies for the gas-sensing performance of S-15 to ppb-level isopropanol were conducted, covering a wide range of test conditions, including temperatures of 240–330 °C and RH of 30–90%. All RH is calculated at 25 °C. The schematic diagram of the resistance changes in response to

isopropanol of S-15 is shown in Fig. 4b. Being n-type metal oxide, the resistance of S-15 significantly increases in the standard air. When isopropanol is injected, the resistance decreases and eventually reaches R_g . The reintroduction of standard air boosts the resistance to a value near R_a . The influences of temperature on the gas-sensing performance of S-15 were analyzed, and the results are shown in Fig. 4c. Sensors coated with S-15 were demonstrated to exhibit the highest response under different concentrations of isopropanol gas at 270 °C, indicating that 270 °C is the optimum temperature suitable for YS-BMO sensors to detect isopropanol gas in low concentrations. Setting the operating temperature at 270 °C can facilitate the dynamics of the reaction of isopropanol adsorption and desorption on YS-BMO, resulting in a marked increase in both response and recovery speeds [43]. Upon studying and analyzing the results shown in Fig. 4b, the t_{res} and t_{rec} of YS-BMO for 1 ppm isopropanol were evaluated to be 10 s and 24.9 s, respectively. The unique inter-shell structure of the sensing materials in YS-BMO may have contributed to the short t_{res} and t_{rec} by enabling the easy diffusion of isopropanol. Furthermore, larger SSA of Bi_2MoO_6 enhances the adsorption rate of VOCs by providing numerous active sites for chemical interaction.

The resistance changes of S-15 (YS-BMO) to 0.1–5 ppm isopropanol at 270 °C and 50% RH, along with its linear relationship of response and concentration, is illustrated in Fig. 4d, e. It is evident that S-15 (YS-BMO) is positively correlated with 0.1–5 ppm isopropanol, and $R^2 = 0.9969$ (0.1–1 ppm) and 0.9985 (1–5 ppm) indicates that it has a high linearity. Response to 5 ppm isopropanol was 6.24, t_{res} and t_{rec} were 10 s and 24.9 s, and actual lowest measured isopropanol concentration was 100 ppb. By utilizing the equation $\text{LOD} = (3\sigma/s)$ provided by Liu et al., we calculated a theoretical limit of detection below 50 ppb [44]. The selectivity of sensors to target gases is a crucial factor for practical

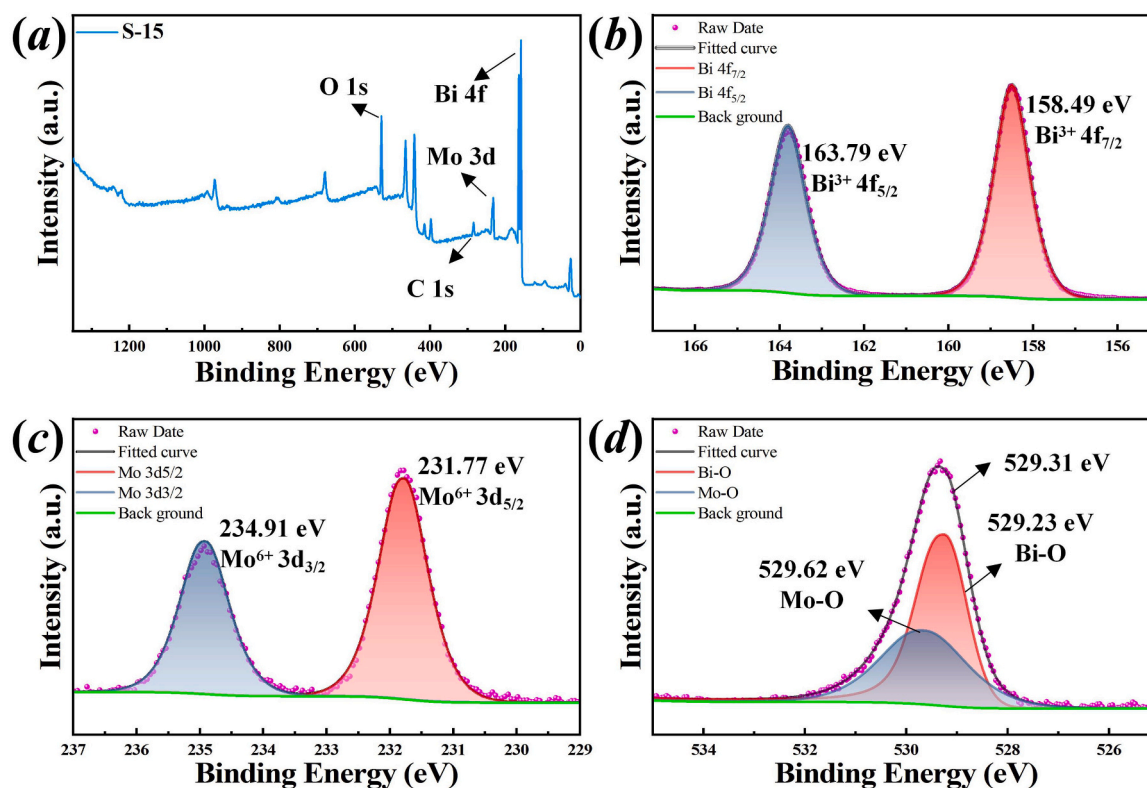


Fig. 3. XPS analysis of S-15: (a) Survey spectra. (b) Bi 4 f spectra. (c) Mo 3d spectra. (d) O 1 s spectra.

applications [4,45]. Fig. 4f illustrates the sensor's sensitivity to different gases (methanol, butanol, formaldehyde, acetone, and ethanol) at a concentration of 5 ppm. Although the sensor exhibits cross-sensitivity to other VOCs, it shows higher sensitivity to isopropanol than other interfering gases due to variations in optimal adsorption and reaction temperatures between VOCs and oxygen species. Hence, YS-BMO demonstrates exceptional selectivity towards isopropanol at its optimal operating temperature of 270 °C. Moreover, the YS-BMO's response to 0.5 ppm of isopropanol was assessed over multiple cycles to ensure repeatability. Fig. 4g displays that the resistance and response values of YS-BMO remained reasonably stable for at least 7 consecutive cycles, with a maximum deviation of 5.02% and a maximum average deviation of only 3.49%, demonstrating the excellent capability for repeating responses to isopropanol. Upon evaluating gas sensors, considering their long-term stability is also crucial. Fig. 4h illustrates the results of the 0.5 ppm isopropanol response tests conducted on the same group of YS-BMO sensors every 7-day intervals. Even after several weeks, YS-BMO maintains stable gas sensitivity to isopropanol. The maximum attenuation of its response to 0.5 ppm isopropanol over 10 weeks was 6.17%, demonstrating its exceptional long-term stability.

Gas sensitivity of MOS sensors is often affected by RH [31]. The gas sensitivity of YS-BMO to 5 ppm isopropanol was investigated under different RH conditions (30%, 50%, 70% and 90%). Fig. 4i indicates that an increase in RH has an insignificant effect (maximum response attenuation <20%) on the isopropanol gas sensitivity of YS-BMO. Interestingly, the reduced response observed with increasing RH proves YS-BMO's isopropanol measurement capability rather than its sensitivity to moisture. This observation is crucial since most MOS sensors have been observed to respond significantly to water vapor alone. Our observation indicates that the humidity-insensitivity of Bi_2MoO_6 is partly attributable to its hydrophobicity, which was discovered incidentally during our preparation process. The hydrophobicity of Bi_2MoO_6 , coupled with a high temperature of 270 °C, impedes water molecules from occupying the adsorption sites that are meant for oxygen ions. Furthermore, the unique layered structure and nanoscale

mesopores of YS-BMO ensure that the Bi_2MoO_6 surface in the yolk-shell remains available for the adsorption of oxygen ions in a high RH. It can be concluded as an outstanding gas-sensing material, which is less-sensitive to humidity. Furthermore, Table 2 provides a comparison of gas sensitivity performance of YS-BMO with other isopropanol sensors, detailing information such as morphology, sensitivity, operating temperature, and RH during isopropanol detection. The experimental results demonstrate that YS-BMO offers obvious gas sensitivity even at lower isopropanol concentrations. As a result, YS-BMO microspheres have shown to be an exceptional gas-sensing material suitable for detecting isopropanol in environments with high levels of humidity.

3.3. DFT and gas-sensing mechanism

DFT was employed to explore the band structure and adsorption properties to systematically examine the response mechanism. The calculation parameters are provided in the "Supplementary Materials". Fig. 5a exhibits the supercell of Bi_2MoO_6 , which consists of 8 Bi, 4 Mo, and 24 O atoms. The optimized lattice parameters ($a=5.807$ Å, $b=16.125$ Å, and $c=5.799$ Å) have been found to possess lower energy when in contrast to the experimental parameters ($a=5.617$ Å, $b=16.625$ Å, $c=5.626$ Å). The (131) plane of the Bi_2MoO_6 was selected as the base plane for investigating isopropanol adsorption for its relatively stable energy compared to (002) [53,54]. Upon adsorption on the Bi_2MoO_6 surface, the isopropanol may be adsorbed onto the top sites of Bi, Mo and O as adsorption model a, b, c. Table 3 lists the calculated adsorption energy (E_{ads}), adsorption distance, and charge transfer values (Q) for models a, b, and c depicted in Fig. 5b-d. Negative adsorption energies values of all models suggest the spontaneous nature of the isopropanol adsorption process. Notably, the adsorption model b demonstrates the lowest adsorption energy of -0.78 eV, indicating that isopropanol is more likely to combine with Mo ions with 2.428 Å. The E_{ads} is calculated by formula (3):

$$E_{ads} = E_{(slab+gas)} - E_{(slab)} - E_{(gas)} \quad (3)$$

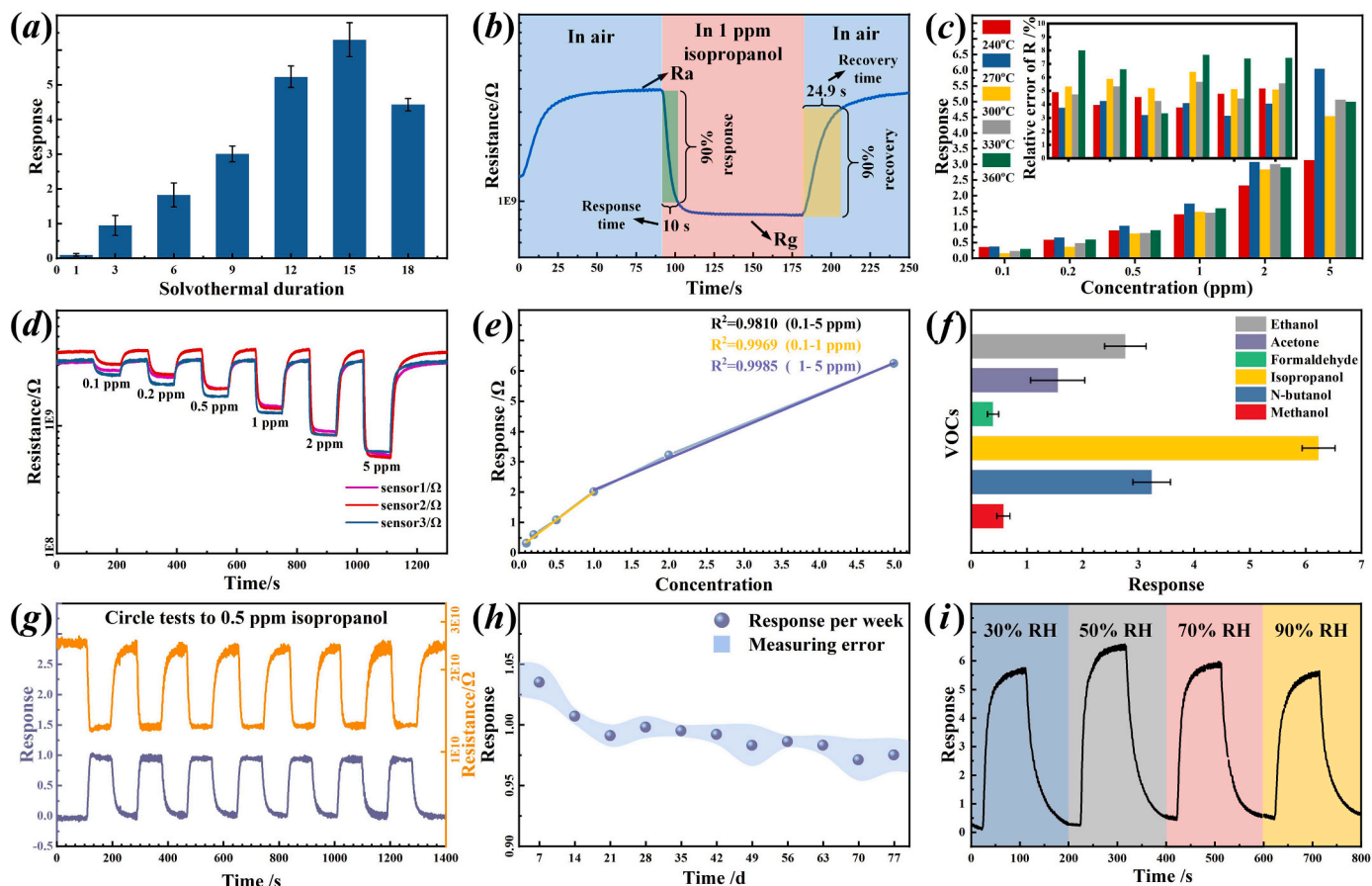


Fig. 4. (a) Influence of solvothermal duration on the gas-sensing performance. (b) The schematic diagram of the resistance changes in response to isopropanol. (c) Influence of working temperature on the gas-sensing performance. (d-e) The resistance changes of the YS-BMO sensor to 0.1–5 ppm isopropanol at 270 °C and linear relationship of response and concentration. (f) Response to various VOC at 5 ppm. (g) Cyclic test of resistance and response. (h) Long-term response and error distribution. (i) Response of YS-BMO to 5 ppm isopropanol under 30%, 50%, 70% and 90% RH at 25 °C.

Table 2

Comparison of different metal oxide-based isopropanol sensors.

Materials	Structure	Operating Temp/°C	RH/%	Concentration/ppm (Response)	t_{res} & t_{rec} /s	REF
Co-ZnO	Nanoflower	225	50	5 (22.5)	330/475	[46]
ZnO-CdO	Coral-like	250	30	100 (17.9)	16/25	[47]
ZnO	Nanoplate	125	0	40 (6.6)	190/200	[48]
NiO/ZnO	Hierarchical	280	-	100 (52.4)	8/50	[49]
MoO ₃ /TiO ₂	Stratiform	RT	50	50 (2.45)	100/40	[50]
/Ti ₃ C ₂ T _x						
Ag-In ₂ O ₃	Hollow sphere	300	0	1 (2.2)	12/175	[4]
Pt-doped SnO ₂	Nanoflowers	250	0	100 (171)	42/7	[51]
Fe-doped ZnO	Nanoneedles	275	50	5 (23.6)	51/762	[52]
QMIM-Bi ₂ MoO ₆	Yolk-shell	270	50	5 (6.2)	15/29	This work
			90	5 (5.2)	27 /36	work

*RT represent room temperature.

whereby, the $E_{(slab)}$ and $E_{(gas)}$ represent the isolated energy of Bi₂MoO₆ (131) and single isopropanol, and $E_{(slab+gas)}$ represents the energy of Bi₂MoO₆ (131)-isopropanol system.

We investigated the band structure and partial density of states (PDOS) of Bi₂MoO₆, as illustrated in Fig. 5e-f. It is obvious that Bi₂MoO₆ is an indirect bandgap semiconductor, where the O 2p orbital occupies the top of the valence band of TDOS, while Bi 6s orbitals slightly contribute to the TDOS near the Fermi energy. The conduction band is mainly filled by hybrid orbitals formed by Mo 4d and O 2p. During the response process of isopropanol adsorption, the electrons transition from hybrid orbitals to 4d orbitals. From the electronic and layered

structure of Bi₂MoO₆, we infer that Bi/Mo sites serve as the reduction reaction site while O sites act as the oxidation reaction sites. 2.365 eV, the theory band gap, is lower than the experimental value of 2.73 eV, which can be understood as the discrepancy caused by the underestimation of the band gap by the GGA-PBE method. The mismatch affirms the logic of our calculations. Furthermore, the conduction band of Bi₂MoO₆ has a higher curvature, indicating a smaller electron effective mass and faster electric carrier speed. The narrow band gap of Bi₂MoO₆ contributes to its enhanced electrical conductivity owing to its reduced transition resistance. The pre-adsorption of O₂ molecules generates O⁻ on the active sites, later displaced by isopropanol molecules bonded to

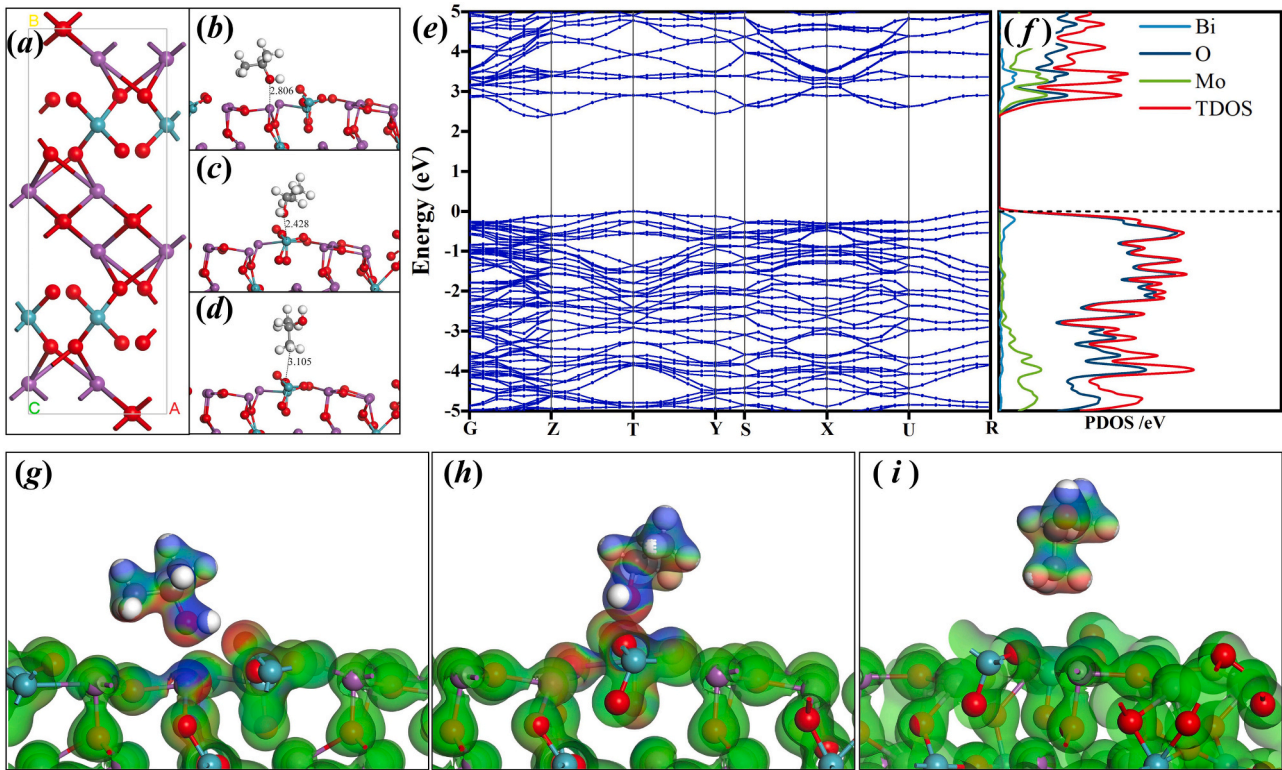


Fig. 5. (a) The super-cell structures of bulk Bi_2MoO_6 (orthorhombic space group Pca21). The optimal isopropanol adsorption models on Bi top (b), Mo top (c) and O top (d). (e) Band structures and (f) Partial Density of States of Bi_2MoO_6 . (g-i) The EDD of the isopropanol-adsorbed on Bi, Mo and O, respectively.

Table 3

The of adsorption performance Isopropanol on Bi_2MoO_6 (131).

Adsorption model	E_{ads}/eV	Distance/ \AA	Charge Transfer/ $ e $
a	-0.574	2.806	2.31
b	-1.934	2.428	1.74
c	-0.334	3.105	0.86

the Bi_2MoO_6 surface. The adsorption and substitution behaviors lead to electron transfer, which significantly alters the sensing material's resistance and forms the sensing mechanism of Bi_2MoO_6 for isopropanol. Besides, the adsorption of isopropanol molecule on the topmost site is profoundly visualized in the charge difference density map (EDD), displaying the charge transfer (Q_t) during molecular adsorption characteristically. The EDD of isopropanol on the top sites of Bi, Mo, and O atoms are illustrated in Fig. 5h-i. In these figures, the blue depicts

electron capture, while the red depicts electron release. After the isopropanol molecule is adsorbed, in all the adsorption configurations, positive charge occurs from the Bi_2MoO_6 (131) to isopropanol. The amount of charge transfer in the adsorption models at the Bi, Mo, and O top sites can be calculated from the change in charge occupancy, which is 2.31 $|e|$, 1.74 $|e|$ and 0.86 $|e|$, respectively. By analyzing the EDD in the adsorption point alone, it is found that charge transfer usually occurs within the hydroxyl group of the isopropanol gas molecule and between ions and O^{2-} . Additionally, the bond length of C-H of the adsorbed isopropanol (1.099 \AA) is smaller than the original bond length of the free isopropanol molecule, while the O-H and C-C bond length have slight increased. The E_{ads} and Q_t of isopropanol on Bi_2MoO_6 were calculated by DFT, and the results of experiments were verified from the point of view of first principles calculation.

As depicted in Fig. 6, the sensing mechanism of YS-BMO to isopropanol was proposed. Its adsorption behavior can be understood by the space charge layer as n-type metal oxide [55]. In brief, when the

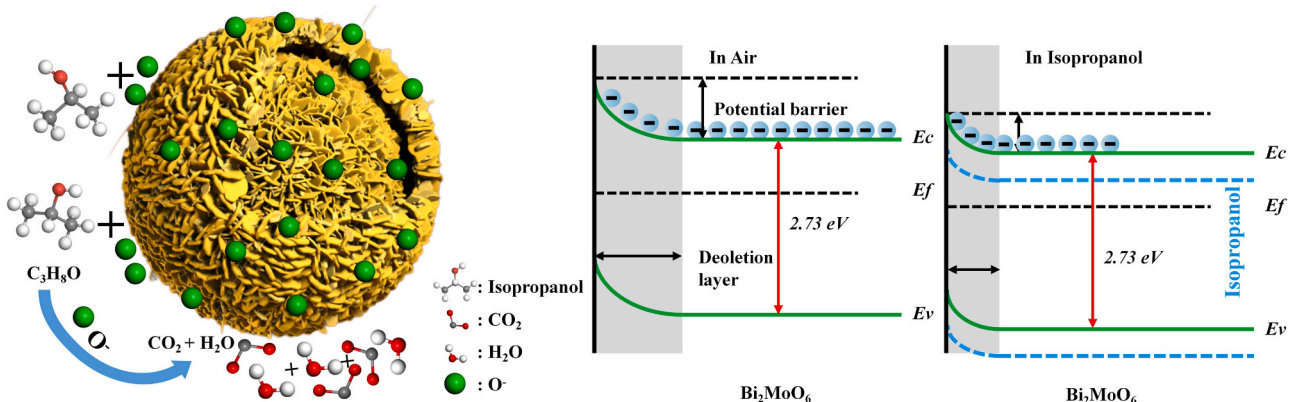
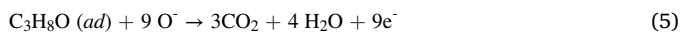


Fig. 6. Schematic of the gas-sensing process of the YS-BMO and band diagram of Bi_2MoO_6 .

adsorbed oxygen captures free e^- from the conduction band of bismuth molybdate at 270 °C, it transforms into O^- , forming a barrier and an electron depletion zone [2]. The decrease in electron concentration in the sensing layer leads to an increase in sensor resistance. Upon the introduction of reductive isopropanol (g), it converts into C_3H_8O (ads) (formula 4), followed by reacting with O^- in a redox reaction to generate CO_2 and H_2O (formula 5). In this process, the previously captured e^- return to Bi_2MoO_6 , shrinking the barrier height and depletion zone thickness, and showing a decrease in resistance.



YS-BMO exhibits exceptional sensing performance with minimal humidity influence in the analysis of low-concentration isopropanol and offers a competent pathway and individual adsorption sites for the transportation and diffusion of isopropanol, subsequently enhancing the response and response speed of Bi_2MoO_6 .

4. Conclusions

This work proposed a straightforward QMIM method based on solvothermal process to prepare YS-BMO gas sensor for detecting ppb-level isopropanol, and comprehensively studied the isopropanol sensing capability of YS-BMO gas sensor. Including $S = 6.24\text{--}5$ ppm isopropanol with t_{res} and t_{rec} of 10 s and 24.9 s, and an actual LOD of 100 ppb. The characterization results indicated that the decent performance of YS-BMO for isopropanol can be attributed to the quasi-molecular imprinting, unique yolk shell structure, open interlayer channels, narrow band gap, and fast-moving charge carriers. DFT calculations also indicated that Bi_2MoO_6 is suitable for the detection of isopropanol. Although the YS-BMO prepared in this work showing considerable gas sensing response to isopropanol at low concentration, the overall isopropanol sensing response to its further application in ppb isopropanol detection in lung cancer diagnosis is still poor. Further mechanism and theoretical analysis need to be studied to guide the gas sensing enhancement of YS-BMO based materials, which is expected to promote the application of gas sensors in the diagnosis of lung cancer and other diseases.

CRedit authorship contribution statement

Chao Zhang: Conceptualization, Supervision, Funding acquisition, Resources, Writing – review & editing. **Xiaoxi He:** Investigation, Writing – original draft. **Yiwen Zhou:** Writing – review & editing. **Jinyong Xu:** Writing – review & editing, Grammar corrections & Editing. **Zichen Zheng:** Writing – review & editing. **Yixiang Bian:** Writing – review & editing. **Marc Debliquy:** Writing – review & editing.

Declaration of Competing Interest

The authors declare that they have no known competing financial interests or personal relationships that could have appeared to influence the work reported in this paper.

Data Availability

Data will be made available on request.

Acknowledgements

This work was supported by the Outstanding Youth Foundation of Jiangsu Province of China under Grant No. BK20211548; the National Natural Science Foundation of China under Grant No. 51872254; the Yangzhou City-Yangzhou University Cooperation Foundation under Grant No. YZ2021153; the Qinglan Project of Yangzhou University.

Appendix A. Supporting information

Supplementary data associated with this article can be found in the online version at [doi:10.1016/j.snb.2023.135059](https://doi.org/10.1016/j.snb.2023.135059).

References

- [1] A. Hasani, H.H. Do, M. Tekalgne, S.H. Hong, H.W. Jang, S.Y. Kim, Recent progress of two-dimensional materials and metal-organic framework-based taste sensors, *J. Korean Ceram. Soc.* 57 (2020) 353–367, <https://doi.org/10.1007/s43207-020-00047-8>.
- [2] X. He, H. Chai, Y. Luo, L. Min, M. Debliquy, C. Zhang, Metal oxide semiconductor gas sensing materials for early lung cancer diagnosis, *J. Adv. Ceram.* 12 (2023) 207–227, <https://doi.org/10.26599/JAC.2023.9220694>.
- [3] H. Chai, Y. Li, Y. Luo, M. Debliquy, C. Zhang, Investigation on isopropanol sensing properties of $LnFeO_3$ ($Ln = Nd, Dy, Er$) perovskite materials synthesized by microwave-assisted hydrothermal method, *Appl. Surf. Sci.* 601 (2022), 154292, <https://doi.org/10.1016/j.apsusc.2022.154292>.
- [4] C. Zhang, Y. Huan, Y. Li, Y. Luo, M. Debliquy, Low concentration isopropanol gas sensing properties of Ag nanoparticles decorated In_2O_3 hollow spheres, *J. Adv. Ceram.* 11 (2022) 379–391, <https://doi.org/10.1007/s40145-021-0530-x>.
- [5] J. Rudnicka, T. Kowalkowski, B. Buszewski, Searching for selected VOCs in human breath samples as potential markers of lung cancer, *Lung Cancer (Amst., Neth.)* 135 (2019) 123–129, <https://doi.org/10.1016/j.lungcan.2019.02.012>.
- [6] M. Hübner, C.E. Simion, A. Tomescu-Stănoiu, S. Pokhrel, N. Bărsan, U. Weimar, Influence of humidity on CO sensing with p-type CuO thick film gas sensors, *Sens. Actuators, B* 153 (2011) 347–353, <https://doi.org/10.1016/j.snb.2010.10.046>.
- [7] M. Hajiali, M. Farhadian, S. Tangestaninejad, M. Khosravi, Synthesis and characterization of Bi_2MoO_6 /MIL-101(Fe) as a novel composite with enhanced photocatalytic performance: effect of water matrix and reaction mechanism, *Adv. Powder Technol.* 33 (2022), 103546, <https://doi.org/10.1016/j.apt.2022.103546>.
- [8] S. Li, C. Wang, Y. Liu, M. Cai, Y. Wang, H. Zhang, Y. Guo, W. Zhao, Z. Wang, X. Chen, Photocatalytic degradation of tetracycline antibiotic by a novel $Bi_2Sn_2O_7$ / Bi_2MoO_6 S-scheme heterojunction: performance, mechanism insight and toxicity assessment, *Chem. Eng. J.* 429 (2022), 132519, <https://doi.org/10.1016/j.cej.2021.132519>.
- [9] T. Yu, Z. Li, S. Chen, Y. Ding, W. Chen, X. Liu, Y. Huang, F. Kong, Facile synthesis of Bi_2MoO_6 hollow microspheres for high-performance supercapacitors, *ACS Sustain. Chem. Eng.* 6 (2018) 7355–7361, <https://doi.org/10.1021/acsschemeng.7b04673>.
- [10] V.-H. Nguyen, H.H. Do, T. van Nguyen, P. Singh, P. Raizada, A. Sharma, S.S. Sana, A.N. Grace, M. Shokouhimehr, S.H. Ahn, C. Xia, S.Y. Kim, Q. van Le, Perovskite oxide-based photocatalysts for solar-driven hydrogen production: progress and perspectives, *Sol. Energy* 211 (2020) 584–599, <https://doi.org/10.1016/j.solener.2020.09.078>.
- [11] C. Cheng, F. Chen, Y. Cheng, G. Lai, Bi_2MoO_6 hierarchical hollow microspheres with remarkable electrochemical performance, *Ceram. Int.* 48 (2022) 26393–26399, <https://doi.org/10.1016/j.ceramint.2022.05.329>.
- [12] Q. Zhang, S. Ma, W. Liu, F. Yuan, A. Alhadi, Significant butanol gas sensor based on unique Bi_2MoO_6 porous microspheres and ZnO nanosheets composite nanomaterials, *J. Alloy. Compd.* 911 (2022), 164877, <https://doi.org/10.1016/j.jallcom.2022.164877>.
- [13] L. He, H. Lv, L. Ma, W. Li, J. Si, M. Ikram, M. Ullah, H. Wu, R. Wang, K. Shi, Controllable synthesis of intercalated γ - Bi_2MoO_6 /graphene nanosheet composites for high performance NO_2 gas sensor at room temperature, *Carbon* 157 (2020) 22–32, <https://doi.org/10.1016/j.carbon.2019.10.011>.
- [14] S. Liu, Y. Qin, J. Xie, Tuning reactivity of Bi_2MoO_6 nanosheets sensors toward NH_3 via Ag doping and nanoparticle modification, *J. Colloid Interface Sci.* 625 (2022) 879–889, <https://doi.org/10.1016/j.jcis.2022.06.026>.
- [15] X. Cui, Y. Xu, X. Zhang, X. Cheng, S. Gao, H. Zhao, L. Huo, In-situ deposited flower-like Bi_2MoO_6 microspheres thin film based sensors for highly selective detection of ppb-level H_2S at low temperature, *Sens. Actuators, B* 247 (2017) 681–690, <https://doi.org/10.1016/j.snb.2017.03.100>.
- [16] F. Zhang, Y. Xu, X. Zhang, L. Sui, P. Hu, Z. Zheng, X. Cheng, S. Gao, H. Zhao, L. Huo, Highly selective ppb-level H_2S sensor based on the walnut-like Bi_2MoO_6 at low temperature, *Sens. Actuators, B* 277 (2018) 312–319, <https://doi.org/10.1016/j.snb.2018.08.151>.
- [17] G. Korotcenkov, Gas response control through structural and chemical modification of metal oxide films: state of the art and approaches, *Sens. Actuators, B* 107 (2005) 209–232, <https://doi.org/10.1016/j.snb.2004.10.006>.
- [18] Z. Zheng, K. Liu, Y. Zhou, M. Debliquy, C. Zhang, Ultrasensitive room-temperature geranyl acetone detection based on $Fe@WO_{3-x}$ nanoparticles in cooked rice flavor analysis, *J. Adv. Ceram.* (2023), <https://doi.org/10.26599/JAC.2023.9220771>.
- [19] T. van Le, Y. Vasseghian, D. van Doan, T.T.T. Nguyen, T.-T. Thi Vo, H.H. Do, K. B. Vu, Q.H. Vu, T. Dai Lam, V.A. Tran, Flexible and high-sensitivity sensor based on Ti_3C_2 - MoS_2 MXene composite for the detection of toxic gases, *Chemosphere* 291 (2022), 133025, <https://doi.org/10.1016/j.chemosphere.2021.133025>.
- [20] B. Li, C. Lai, M. Zhang, S. Liu, H. Yi, X. Liu, N. An, X. Zhou, L. Li, Y. Fu, L. Qin, L. Chen, N. S-GQDs and Au nanoparticles Co-modified ultrathin Bi_2MoO_6 nanosheet with enhanced charge transport dynamics for full-spectrum-light-driven molecular oxygen activation, *Chem. Eng. J.* 409 (2021), 128281, <https://doi.org/10.1016/j.cej.2020.128281>.

- [21] Y. Li, Y.-L. Lu, K.-D. Wu, D.-Z. Zhang, M. Debliquy, C. Zhang, Microwave-assisted hydrothermal synthesis of copper oxide-based gas-sensitive nanostructures, *Rare Met* 40 (2021) 1477–1493, <https://doi.org/10.1007/s12598-020-01557-4>.
- [22] H.H. Do, J.H. Cho, S.M. Han, S.H. Ahn, S.Y. Kim, Metal-organic-framework- and mxene-based taste sensors and glucose detection, *Sensors* 21 (2021), <https://doi.org/10.3390/s21217423>.
- [23] S.H. Narwade, P.V. Shinde, N.M. Shinde, V.V. Jadhav, S.F. Shaikh, R.S. Mane, U. V. Bhosle, Hydrangea-type bismuth molybdate as a room-temperature smoke and humidity sensor, *Sens. Actuators, B* 348 (2021), 130643, <https://doi.org/10.1016/j.snb.2021.130643>.
- [24] C. Zhang, J. Xu, H. Li, H. Liao, Role of ruthenium incorporation on room-temperature nonanal sensing properties of Ru-loaded urchin-like $W_{18}O_{49}$ hierarchical nanostructure, *Sens. Actuators, B* 353 (2022), 131096, <https://doi.org/10.1016/j.snb.2021.131096>.
- [25] F. Zhang, X. Dong, X. Cheng, Y. Xu, X. Zhang, L. Huo, Enhanced gas-sensing properties for trimethylamine at low temperature based on $MoO_3/Bi_2Mo_3O_{12}$ hollow microspheres, *ACS Appl. Mater. Interfaces* 11 (2019) 11755–11762, <https://doi.org/10.1021/acsami.8b22132>.
- [26] K.-D. Wu, J.-Y. Xu, M. Debliquy, C. Zhang, Synthesis and NH_3/TMA sensing properties of $CuFe_2O_4$ hollow microspheres at low working temperature, *Rare Met* 40 (2021) 1768–1777, <https://doi.org/10.1007/s12598-020-01609-9>.
- [27] C. Zhang, K. Liu, Z. Zheng, M. Debliquy, Defect engineering of nanostructured $ZnSnO_3$ for conductometric room temperature CO_2 sensors, *Sens. Actuators, B* 384 (2023), 133628, <https://doi.org/10.1016/j.snb.2023.133628>.
- [28] J. Li, X. Liu, Z. Sun, L. Pan, Mesoporous yolk-shell structure Bi_2Mo_6 microspheres with enhanced visible light photocatalytic activity, *Ceram. Int.* 41 (2015) 8592–8598, <https://doi.org/10.1016/j.ceramint.2015.03.068>.
- [29] B. Wang, Q. Yu, S. Zhang, T. Wang, P. Sun, X. Chuai, G. Lu, Gas sensing with yolk-shell $LaFeO_3$ microspheres prepared by facile hydrothermal synthesis, *Sens. Actuators, B* 258 (2018) 1215–1222, <https://doi.org/10.1016/j.snb.2017.12.018>.
- [30] C.A. Zito, T.M. Perfecto, A.-C. Dippel, D.P. Volanti, D. Koziej, Low-temperature carbon dioxide gas sensor based on yolk-shell ceria nanospheres, *ACS Appl. Mater. Interfaces* 12 (2020) 17745–17751, <https://doi.org/10.1021/acsami.0c01641>.
- [31] Y. Xiong, Z. Zhu, D. Ding, W. Lu, Q. Xue, Multi-shelled $ZnCo_2O_4$ yolk-shell spheres for high-performance acetone gas sensor, *Appl. Surf. Sci.* 443 (2018) 114–121, <https://doi.org/10.1016/j.apsusc.2018.02.189>.
- [32] L. Wang, Z. Lou, J. Deng, R. Zhang, T. Zhang, Ethanol gas detection using a yolk-shell (Core-Shell) $\alpha-Fe_2O_3$ nanospheres as sensing material, *ACS Appl. Mater. Interfaces* 7 (2015) 13098–13104, <https://doi.org/10.1021/acsami.5b03978>.
- [33] R. Zhang, T. Zhang, T. Zhou, L. Wang, Rapid sensitive sensing platform based on yolk-shell hybrid hollow sphere for detection of ethanol, *Sens. Actuators, B* 256 (2018) 479–487, <https://doi.org/10.1016/j.snb.2017.10.064>.
- [34] K. Wu, Y. Luo, Y. Li, C. Zhang, Synthesis and acetone sensing properties of $ZnFe_2O_4/rGO$ gas sensors, *Beilstein J. Nanotechnol.* 10 (2019) 2516–2526, <https://doi.org/10.3762/bjnano.10.242>.
- [35] C. Zhang, Y. Li, G. Liu, K. Liu, K. Wu, Room temperature NO_2 sensing properties of ZnO_{1-x} coating prepared by hydrogen reduction method, *Ceram. Int.* 47 (2021) 29873–29880, <https://doi.org/10.1016/j.ceramint.2021.07.160>.
- [36] C. Zhang, Y. Li, G.-F. Liu, H.-L. Liao, Preparation of ZnO_{1-x} by peroxide thermal decomposition and its room temperature gas sensing properties, *Rare Met* 41 (2022) 871–876, <https://doi.org/10.1007/s12598-021-01840-y>.
- [37] W.Q. Fang, X.H. Yang, H. Zhu, Z. Li, H. Zhao, X. Yao, H.G. Yang, Yolk@shell anatase TiO_2 hierarchical microspheres with exposed {001} facets for high-performance dye sensitized solar cells, *J. Mater. Chem.* 22 (2012) 22082, <https://doi.org/10.1039/c2jm34787c>.
- [38] X. Meng, Z. Zhang, Pd-doped Bi_2Mo_6 plasmonic photocatalysts with enhanced visible light photocatalytic performance, *Appl. Surf. Sci.* 392 (2017) 169–180, <https://doi.org/10.1016/j.apsusc.2016.08.113>.
- [39] H. Li, Z. Bian, J. Zhu, D. Zhang, G. Li, Y. Huo, H. Li, Y. Lu, Mesoporous titania spheres with tunable chamber structure and enhanced photocatalytic activity, *J. Am. Chem. Soc.* 129 (2007) 8406–8407, <https://doi.org/10.1021/ja072191c>.
- [40] K. Wu, H. Chai, K. Xu, M. Debliquy, C. Zhang, Effect of {010} crystal facets of Bi_2Mo_6 and 1D/2D heterostructures for conductometric room temperature NH_3 gas sensors, *Sens. Actuators, B* 376 (2023), 132983, <https://doi.org/10.1016/j.snb.2022.132983>.
- [41] Z. Zheng, Y. Li, Y. Luo, M. Debliquy, C. Zhang, Facile synthesis of bismuth ferrite nanoparticles for ppm-level isopropanol gas sensor, *J. Mater. Sci. Mater. Electron.* 33 (2022) 18507–18521, <https://doi.org/10.1007/s10854-022-08703-x>.
- [42] X. Zhou, X. Cheng, Y. Zhu, A.A. Elzattary, A. Alghamdi, Y. Deng, D. Zhao, Ordered porous metal oxide semiconductors for gas sensing, *Chin. Chem. Lett.* 29 (2018) 405–416, <https://doi.org/10.1016/j.ccl.2017.06.021>.
- [43] B. Saruhan, R. Lontio Fomekong, S. Nahiriak, Review: influences of semiconductor metal oxide properties on gas sensing characteristics, *Front. Sens.* 2 (2021) 2, <https://doi.org/10.3389/fsens.2021.657931>.
- [44] J. Liu, L. Zhang, B. Cheng, J. Fan, J. Yu, A high-response formaldehyde sensor based on fibrous $Ag-ZnO/In_2O_3$ with multi-level heterojunctions, *J. Hazard. Mater.* 413 (2021), 125352, <https://doi.org/10.1016/j.jhazmat.2021.125352>.
- [45] J. Xu, C. Zhang, Oxygen vacancy engineering on cerium oxide nanowires for room-temperature linalool detection in rice aging, *J. Adv. Ceram.* 11 (2022) 1559–1570, <https://doi.org/10.1007/s40145-022-0629-8>.
- [46] Y. Luo, A. Ly, D. Lahem, J.D. Martin, A.-C. Romain, C. Zhang, M. Debliquy, Role of cobalt in Co-ZnO nanoflower gas sensors for the detection of low concentration of VOCs, *Sens. Actuators, B* 360 (2022), 131674, <https://doi.org/10.1016/j.snb.2022.131674>.
- [47] X. Cai, D. Hu, S. Deng, B. Han, Y. Wang, J. Wu, Y. Wang, Isopropanol sensing properties of coral-like $ZnO-CdO$ composites by flash preparation via self-sustained decomposition of metal-organic complexes, *Sens. Actuators, B* 198 (2014) 402–410, <https://doi.org/10.1016/j.snb.2014.03.093>.
- [48] I. kortidis, S. Lushozi, N. Leshabane, S.S. Nkosi, O.M. Ndwandwe, J. Tshilongo, N. Ntsasa, D.E. Motaung, Selective detection of propanol vapour at low operating temperature utilizing ZnO nanostructures, *Ceram. Int.* 45 (2019) 16417–16423, <https://doi.org/10.1016/j.ceramint.2019.05.172>.
- [49] S.-C. Wang, X.-H. Wang, G.-Q. Qiao, X.-Y. Chen, X.-Z. Wang, N.-N. Wu, J. Tian, H.-Z. Cui, NiO nanoparticles-decorated ZnO hierarchical structures for isopropanol gas sensing, *Rare Met* 41 (2022) 960–971, <https://doi.org/10.1007/s12598-021-01846-6>.
- [50] Y. Yao, Y. Han, M. Zhou, L. Xie, X. Zhao, Z. Wang, N. Barsan, Z. Zhu, $MoO_3/TiO_2/Ti_3C_2T_x$ nanocomposite based gas sensors for highly sensitive and selective isopropanol detection at room temperature, *J. Mater. Chem. A* 10 (2022) 8283–8292, <https://doi.org/10.1039/D1TA11018G>.
- [51] W. Bi, W. Xiao, S. Liu, Synthesis of Pt-doped SnO_2 flower-like hierarchical structure and its gas sensing properties to isopropanol, *J. Mater. Sci.* 56 (2021) 6095–6109, <https://doi.org/10.1007/s10853-020-05655-7>.
- [52] Y. Luo, A. Ly, D. Lahem, C. Zhang, M. Debliquy, A novel low-concentration isopropanol gas sensor based on Fe-doped ZnO nanoneedles and its gas sensing mechanism, *J. Mater. Sci.* 56 (2021) 3230–3245, <https://doi.org/10.1007/s10853-020-05453-1>.
- [53] Y. Qin, S. Liu, X. Shen, H. Gui, Y. Bai, Enhanced gas sensing performance of Bi_2Mo_6 with introduction of oxygen vacancy: Coupling of experiments and first-principles calculations, *J. Alloy. Compd.* 894 (2022), 162534, <https://doi.org/10.1016/j.jallcom.2021.162534>.
- [54] S. Zhang, W. Pu, A. Chen, Y. Xu, Y. Wang, C. Yang, J. Gong, Oxygen vacancies enhanced photocatalytic activity towards VOCs oxidation over Pt deposited Bi_2WO_6 under visible light, *J. Hazard. Mater.* 384 (2020), 121478, <https://doi.org/10.1016/j.jhazmat.2019.121478>.
- [55] B. Yu, W. Yan, Y. Meng, Y. Zhang, X. Li, Y. Li, Y. Zhong, J. Ding, H. Zhang, Selected dechlorination of triclosan by high-performance $g-C_3N_4/Bi_2Mo_6$ composites: mechanisms and pathways, *Chemosphere* 312 (2023), 137247, <https://doi.org/10.1016/j.chemosphere.2022.137247>.

Chao Zhang received a B.S. degree from the Chongqing University (China) in 2003 and a joint Ph.D. degree from Technology University of Belfort-Montbéliard (France) and Xi'an Jiaotong University (China) in June 2008. From September 2007 to January 2009, he worked as a teaching-research assistant in Technology University of Belfort-Montbéliard. Since Feb 2009, he is postdoctoral researcher, and then a senior researcher in Materials Science Department of engineering School of University of Mons (Belgium). In 2014, he joined Yangzhou University (China) as professor where he is leading a research group on thermal spray coatings and gas sensors. He is Vice Dean (August 2016 to September 2022) and Dean (September 2022 to present) of College of Mechanical Engineering. His research interests include thermal-sprayed techniques and coatings, especially gas sensing and wear-resistant coatings.

Xiaoxi He received his B.S. degree in 2021 at Southwest University of Science and Technology (China). He is currently pursuing his Ph.D. degree at Yangzhou University (China). He takes interests in smart materials for high-performance gas sensors for lung cancer detection.

Yiwen Zhou received her B.S. degree in 2022 at Yangzhou University (China). She is currently pursuing her M.D. degree at Yangzhou University (China). She takes interests in smart materials for high-performance gas sensors for factory toxic gas detection.

Jinyong Xu received his B.S. degree in 2018 at Shanghai Institute of Technology (China). He is currently a Ph.D. student at Yangzhou University, and takes an interest in smart materials for high-performance gas sensors.

Zichen Zheng received his B.S. degree in 2020 at Hefei University of Technology (China). He is currently pursuing his Ph.D. degree at Yangzhou University (China). He takes interests in smart materials for high-performance gas sensors working at room temperature.

Yixiang Bian received his Ph.D. at Nanjing University Of Aeronautics and Astronautics in the field of Testing and Metrology Technology and Instruments. He joined Yangzhou University in 2009. He is responsible for research activities in the field of insect hair receptors and biological perception mechanisms.

Marc Debliquy received his Ph.D. at Faculty of Engineering in Mons (Belgium) in 1999 in the field of organic semiconductors for fire detection. He joined the Sochinor Company in 2000. He left in 2003 for joining Materia Nova. He was responsible for the research activities in the field of gas sensors. Since October 2008, he joined the Material Science Department of Faculty of Engineering of University of Mons and worked as a team leader of semiconductor and sensor group. He was promoted as associate professor in September 2013. His main research interest is smart coatings for chemical detection.